Retrieval of Normalized Gamma Size Distribution Parameters using Precipitation Imaging Package (PIP) Snowfall Observations during ICE-POP 2018

Ali Tokay*
Joint Center for Earth Systems Technology, University of Maryland Baltimore County and
NASA Goddard Space Flight Center, Greenbelt, MD
Liang Liao
Morgan State University and NASA Goddard Space Flight Center, Greenbelt, MD
Robert Meneghini
NASA Goddard Space Flight Center, Greenbelt, MD
Charles N. Helms
Earth System Science Interdisciplinary Center, University of Maryland and
NASA Goddard Space Flight Center, Greenbelt, MD
S. Joseph Munchak
NASA Goddard Space Flight Center, Greenbelt, MD
David B. Wolff
NASA Goddard Space Flight Center Wallops Flight Facility, Wallops Island, VA
Patrick N. Gatlin
NASA Marshall Space Flight Center, Huntsville, AL

Submitted to Journal of Applied Meteorology and Climatology
December 28, 2021
Revised March 13, 2022
Revised July 8, 2022
Revised December 26,2022
Accepted February 9, 2023

*Corresponding Author:
Mesoscale Processes Laboratory (Code 612.0),
NASA Goddard Space Flight Center, Greenbelt, MD 20771
tokay@umbc.edu

Abstract

Parameters of the normalized gamma particle size distribution (PSD) have been retrieved from the Precipitation Image Package (PIP) snowfall observations collected during the International Collaborative Experiment - PyeongChang Olympics and Paralympic (ICE-POP 2018). Two of the gamma PSD parameters, the mass weighted particle diameter (D_{mass}) and the normalized intercept parameter N_W, have median values of 1.15-1.31 mm and 2.84-3.04 log(mm^{-1} m^{-3}), respectively. This range arises from the choice of the relationship between the maximum versus equivalent diameter, D_{mx}-D_{eq}, and the relationship between the Reynolds and Best numbers, *Re-X*. Normalization of snow water equivalent rate (SWER) and ice water content (W) by N_W reduces the range in N_W resulting in well fitted power law relationship, between SWER/N_W and D_{mass} and between W/N_W and D_{mass}. The bulk descriptors of snowfall are calculated from PIP observations and from the gamma PSD with values of the shape parameter (μ) ranging from -2 to 10. NASA's Global Precipitation Measurement (GPM) mission, which adopted the normalized gamma PSD, assumes $\mu = 2$ and $\mu = 3$ in its two separate algorithms. The mean fractional bias (MFB) of the snowfall parameters changes with μ, where the functional dependence on μ depends on the specific snowfall parameter of interest. The MFB of the total concentration was underestimated by 0.23-0.34 when $\mu = 2$ and by 0.29-0.40 when $\mu = 3$, while the MFB of SWER had a much narrower range (-0.03 to 0.04) for the same μ values.

1. Introduction

The particle size distribution (PSD) is a critical descriptor of falling snow and provides a means to derive the total concentration (N_T), the snow water equivalent rate (SWER), and the equivalent radar reflectivity (Ze). The accuracy of PSD measurement depends on the accuracy of particle size and concentration measurements in a given volume. The bulk descriptors of falling snow also depend on the fall velocity measurements.

The Precipitation Imaging Package (PIP) is an instrument designed to measure size, concentration, and fall velocity of precipitating particles. The instrument has seen wide use since its introduction (Newman et al. 2009) and has been improved through several hardware and software upgrades by the instrument inventor, Dr. Larry F. Bliven of NASA Wallops Flight Facility (Pettersen et al. 2020a). A direct comparison between the PIP-calculated and gauge- or stake field-measured snow water equivalent (SWE) provides critical information on the accuracy of the PIP measurements. Figure 2a of von Lerber et al. (2017) shows excellent agreement in SWE calculated from the PIP versus a reference Pluvio^2-200 weighing bucket gauge-based SWE within double wind fence in Finland. The total accumulation calculated from the PIP was within 5% for three different particle mass calculation methods. Pettersen et al. (2020b) demonstrated that the PIP-derived bulk liquid water equivalent accumulation was within 2.5% of that from a co-located snow stake field over several snowfall events. Tokay et al. (2022) reported less than 15% absolute bias between the PIP-calculated and stake field measured SWE for each of 30 snow events. The Pettersen et al. (2020b) and Tokay et al. (2022) studies were both conducted using the PIP dataset from Marquette, Michigan but used different methods for estimating SWE from the snow particle measurements. This study uses the methodology described in Tokay et al. (2022) for the snowflake mass calculation.

The three-parameter gamma distribution has been widely used to parameterize the PSDs from aerosol and cloud droplets to liquid and frozen precipitation particles (Petty and Huang 2011 and references therein). The precipitation retrieval algorithms used for the NASA's Global Precipitation Measurement (GPM) mission core satellite active and passive sensors

87 are no exception (Skofronick-Jackson et al. 2017). The GPM dual-frequency precipitation
88 radar (DPR) and combined radar-radiometer algorithms have adopted a normalized gamma
89 particle size distribution defined by mass weighted particle diameter (D_{mass}), normalized
90 intercept parameter (N_W) and the shape parameter (μ) (Grecu et al. 2016, Seto et al. 2021).
91 The shape parameter is assumed to be constant with $\mu = 2$ for the combined radiometer-
92 radar algorithm (Grecu et al. 2016) and $\mu = 3$ for the DPR algorithm (Iguchi et al. 2017).
93
94 The retrieval of D_{mass} and N_W from DPR algorithms involves six different modules that were
95 shown by a flow chart in Figure 2 of Seto et. al. (2021). One of modules, the PSD module,
96 uses a power law relationship between the precipitation rate (PR) and D_{mass} as a constraint
97 for the size distribution. The coefficient and exponent of the PR(D_{mass}) relationship rely on
98 the coefficient and exponent of the k(Ze) relationship, where k is the specific attenuation and
99 the relationship was calculated for Ku-band (Kozu et al. 2009). The k(Ze) relationship was
100 derived for the analysis of data from the Ku-band radar onboard the Tropical Rainfall
101 Measuring Mission (TRMM) satellite, the predecessor of GPM, and was based on disdrometer
102 measurements in the tropics. Under the GPM ground validation program, Chase et al. (2020)
103 revisited the PR(D_{mass}) relationship using the PIP snowfall observations from Finland and
104 found that the DPR PR(D_{mass}) relationship is not optimum for snowfall. It should be noted
105 that the PR(D_{mass}) relationship is based on the melted mass weighted particle diameter,
106 D_{mass}*.
107
108 The probability distributions of D_{mass}, log(N_W), and μ in rain (Tokay and Bashor 2010, Tokay
109 et al. 2016, 2017) and the two-dimensional histograms of log(N_W) versus D_{mass} (Liao et. al.
110 2020, Tokay et al. 2020) have been derived through the use of disdrometer measurements.
111 Despite these studies, there are a few observational studies focusing on the PSD parameters
112 of the falling snow. Using the PIP PSD observations from NASA Wallops Flight Facility,
113 Wallops Island, Virginia, Liao et al. (2016) concluded that the exponential PSD model ($\mu = 0$)
114 is sufficiently accurate for the dual-wavelength radar retrieval of snow bulk parameters.
115 Using the PIP PSD observations from Marquette, Michigan, Pettersen et al. (2020a) and Kulie
116 et al. (2021) showed noticeable differences in the two-dimensional histogram of the

intercept and slope parameters of exponential PSD between the deep and shallow snow events. Yu et al. (2020) presented the probability distributions of D_{mass} and $\log(N_W)$ at different snow density intervals using the Particle Size Velocity (PARSIVEL^2) disdrometer measurements collected during the International Collaborative Experiment – PyeongChang Olympic and Paralympic (ICE-POP 2018) in South Korea. The distributions of D_{mass} and $\log(N_W)$ shifted toward lower and higher values, respectively with increasing snow density. It should be noted that the snow density refers to the bulk density of falling snow within a volume; not the density of the individual snowflakes.

This study uses the PIP observations from the ICE-POP 2018 field campaign to derive the parameters of the normalized gamma PSD in snow. It has two main objectives: 1) To provide a reference for the range of D_{mass} and $\log(N_W)$ observations in snow and their dependence on snow density (ρ_{snow}), Ku-band reflectivity (Ze_{ku}), and DFR; 2) To evaluate the performance of the prescribed μ of the gamma PSD, particularly for $\mu = 2$ and $\mu = 3$. The observation-based database makes this study *original* and complements the Liao et al. (2016) study which is primarily based on theoretical calculations. The D_{mass} and $\log(N_W)$ are retrieved from the GPM DPR algorithm and the library of the expected statistics of these parameters from in-situ observations in snow is evidence of the *practical significance* of the study.

The manuscript is organized as follows. The instrumentation, and the database are summarized in Section 2. Section 3 is dedicated to the methodology where the calculation procedure and formulations for particle mass and bulk descriptors of snowfall are laid out. As mentioned, the methodology of this study is based on Tokay et al. (2022), and critical points are repeated here for the readers' convenience. The results can be found in Section 4 followed by summary and conclusions in Section 5.

2.Observations

a. Measurement Site

147 ICE-POP 2018 is one of the major recent efforts to characterize the winter weather in
148 complex terrain (Tapiador et al. 2021). A number of ground sites were located along the
149 Pacific coast of South Korea and inland in the mountainous regions. The inland sites
150 gathered detailed measurements within complex terrain. The PIP sites, for example, were at
151 175 m and 789 m above the mean sea level. The precipitation at the lower elevation site was
152 dominated by liquid and mixed phase, while the higher elevation site received abundant
153 snowfall over a wide range of cold temperatures ($0^{\circ}C \geq T_{wb} \geq -13^{\circ}C$; T_{wb}: wet bulb
154 temperature). This study uses the PIP observations from the higher elevation site, the
155 MayHills supersite (MHS; 37.6652˚N, 128.6996 ˚E). The MHS site had a wealth of in-situ and
156 remote sensing instrumentation including a W-band profiler, a Multi-Angle Snowflake
157 Camera (MASC), a two-dimensional video disdrometer (2DVD) (Gehring et al. 2021), and a
158 PARSIVEL^2 disdrometer (Yu et al. 2020).
159
160 b. Instrumentation
161
162 This study primarily uses PIP to calculate the particle mass, PSD, and bulk descriptors of
163 snowfall (Figure 1a). The Vaisala WXT520 weather station provided additional
164 measurements needed for the computation of the particle mass and the determination of
165 snowing minutes ($T_{wb} \leq 0^{\circ}C$) (Figure 1b). A third key instrument in this study was the
166 PARSIVEL^2, a present weather sensor that is used here to verify the snowing minutes
167 determination made by the WXT520. An important limitation of the PARSIVEL^2 is that the
168 instrument sometimes reports drizzle in the presence of light snow. This limitation, however,
169 should have minimal impact on this study. PARSIVEL^2 measures the size and fall velocity
170 of snowflakes but the size cannot be interpreted as the equivalent diameter of the complex
171 shape of snowflakes. The measurement uncertainty of PARSIVEL^2's fall velocity was
172 previously reported by Tokay et al. (2014) in rain and the issue is valid for snowfall. In short,
173 PIP is superior to PARSIVEL^2 for particle size and fall velocity measurements in snow. Here,
174 the working principles, measured quantities (e.g. size, fall velocity), and data output of PIP
175 are briefly described and follows closely the description given in Tokay et al. (2022).
176





Figure 1. Picture of a) Precipitation Imaging Package (PIP), b) Vaisala WXT520 weather station from MHS supersite (Courtesy of Kwonil Kim of Kyungpook National University).

PIP (Pettersen et al. 2020b, 2021) is a digital video disdrometer developed as a successor to the Snow Video Imager (SVI; Newman et al. 2009). The instrument is composed of a high-speed video camera and a light source located 2 m apart with a focal plan located approximately 1.3 m from the camera lens. This open sample volume setup makes PIP measurements highly resistant to contamination from secondary particles generated by shattering as well as to under-sampling in windy conditions. Although windy conditions can

introduce motion blurring, the relative impact on the particle measurements has been found to be minor (Helms et al. 2022). Data is collected in the form of two-dimensional grayscale video at a rate of 380 frames per second with an image size of 640 by 480 pixels. Given a calibrated pixel size of 0.1 mm by 0.1 mm, the image represents a 64 mm by 48 mm field of view (FOV). Since particle that intersect the edge of this FOV are ignored, however, the actual sampling region FOV will be smaller than the full 64 mm by 48 mm FOV. The complete sampling volume will be a multiplication of this smaller particle-size-dependent FOV, a particle-size-dependent depth of field (DOF), and the number of frames over a given time period.

Although the calibrated pixel size for PIP is 0.1 mm by 0.1 mm, the instrument uses custom image compression to handle the high data rates produced by the high speed camera. This image compression works by averaging vertically-adjacent pairs of pixels prior to transmission and assigning that average to both the pixels composing the pair after transmission. As a result, the effective pixel size is 0.1 mm by 0.2 mm when considering resolution effects. To this end, only particles with an equivalent diameter (D_{eq}) of at least 0.2 mm are considered to prevent camera resolution and image compression issues from contaminating the size distributions. While Newman et al. (2009) reported the standard sizing error of SVI to be approximately 18%, the PIP setup uses a DOF that is half the size of the SVI DOF to reduce the uncertainty in the size measurements.

Generating particle measurements from the PIP images is handled via the National Instruments Image Acquisition (IMAQ, 2004) software package. One of the major improvements from SVI to PIP is that PIP is able to measure the fall velocity of individual particles (Pettersen et al. 2020b) by using the IMAQ object tracking software to determine particle motion over the span of multiple images.

In addition to particle motion, the IMAQ software package also produces multiple measures of particle shape and size. Recent work (Helms et al. 2022) has found that PIP estimates of particle maximum dimension (D_{mx}), which are computed by fitting an ellipse to the PIP-imaged particle, are unreliable due to the specific method the software uses to produce the

ellipse fit. The PIP ellipse-fitted method that is currently (as of PIP software revision 1506) used performs the shape fitting by defining the fitted ellipse to have equal perimeter and area to the observed particle; no information about the pixel spatial distribution within the particle (i.e., the particle shape) is considered when making this fit. Although Helms et al. (2022) demonstrated that the data could be reprocessed using a more reliable shape fitting algorithm, reprocessing the data is beyond the scope of the present study. As such, the present study will estimate an appropriate D_{mx} from the Waddel disk diameter.

The Waddel disk diameter (D_{eq}) is defined as the diameter of the disk with the same area as the particle. It is equal to $2(\text{area}/\pi)^{0.5}$, where the area is the total area of the shadowed pixels bounded by a box (see Table 10-1 of the IMAQ vision concepts manual; IMAQ, 2004). The D_{mx} is expressed as a function of D_{eq} as described in the methodology section. Figure 1b of von Lerber et al. (2017) shows the schematic image of a plane projection of a PIP-observed snowflake, as viewed from the side, with annotations indicating D_{eq} and D_{mx}.

The PIP velocity files are generated independently of the particle files that are used to construct the PSD. They include the time stamp of D_{eq} and the fall velocity of the particles. While most particles have positive fall velocities, it is feasible that the particle may have a negative fall velocity, indicating upward motion. To exclude upward-moving particles, only particles with a downward vertical velocity greater than 0 m s^{-1} are included in the analysis.

c. Database

This study uses a composite of 10 snow events over the Korean Peninsula that were recorded by the PIP during the first three months of 2018. The events are the combination of cold low (4 events), warm low (5 events), and air-sea interaction (1 event) events described in Kim et al. (2021). The PSD characteristics of air-mass interaction event was in line with the warm low events. The combined snow events resulted in a geometric snow depth of 1524 mm (60 inches) over 8,230 minutes.

3.Methodology

This section describes the procedure for determining the three parameters of the normalized gamma PSD from the PIP particle size, and velocity measurements. The choice of the prescribed D_{mx}-D_{eq} relationship and the four different approaches of particle mass calculation play important roles in determining the PSD parameters.

a. Snowflake Mass

The particle mass was calculated from PIP measurements by using the hydrometeor aerodynamics outlined by Böhm (1989, BM hereafter). A similar approach was previously used by Szyrmer and Zawadzki (2010), von Lerber et al. (2017), and Tokay et al. (2022) and the four-step process that is used in this study follows that of Tokay et al. (2022). In brief, the D_{mx} is prescribed as a function of the D_{eq};

$$D_{mx} = \alpha D_{eq} \quad (1)$$

where α = 1.1, 1.2, 1.3, and 1.4 following Moisseev et al. (2017), von Lerber et al. (2018) and recent work by Helms et al. (2022). First, For each five-minute interval, the PIP fall velocity measurements are binned into 0.2-mm-wide D_{mx} bins whose midpoints ranged from 0.1 mm to 19.9 mm. As was the case in Tokay et al. (2022), the median fall velocity (v) of each bin, rather than the mean fall velocity of each bin, is used here because the fall velocity measurements does not necessarily follow a normal distribution within each bin. The fall velocity distributions deviate from normal distributions mainly due to the presence of higher fall speed outliers as described in Tiira et al. (2016).

Second, the median fall velocity and the corresponding midpoint of the D_{mx} bin are used to calculated the Reynolds number (Re) for each bin using the following equation,

$$Re = v\, D_{mx}\, \rho_a / \eta \quad (2)$$

where ρ_a and η are the density of air and the dynamic viscosity, respectively, and are computed from observations collected by the Vaisala WXT520 weather station collocated at the site.

Third, the Best number (X), also known as Davies number, is calculated from Re for each size bin and is expressed as

$$X = \left(\frac{\delta_0^2 C_0^{\frac{1}{2}}}{4}\left\{\left[\frac{(4Re)^{\frac{1}{2}}}{\delta_0} + 1\right]^2 - 1\right\}\right)^2 \quad (3)$$

where δ_0, and C_0 are the boundary layer thickness and the drag coefficient and are taken as 5.83 and 0.6, respectively following Böhm (1989). Eq. (3) is a generalized theoretical relationship between Re and X considering idealized spheroidal snowflake shapes. Mitchell and Heymsfield (2005, MH hereafter) and Khvorostyanov and Curry (2005, KC hereafter) offered an alternative *Re-X* relationship for a turbulence correction to increase the drag at very large Re in the presence of large aggregates. Szyrmer and Zawadzki (2010) provided a reformulation of the MH and KC relationships in the form of an eighth-order polynomial and it is their reformulations that will be used in this study, although the relationships will still be referred to as MH and KC, respectively. Heymsfield and Westbrook (2010, HW hereafter) sought a better agreement between the observed and theoretical fall velocities in the presence of pristine ice crystals and aggregates. They suggested $\delta_0 = 8.0$ and $C_0 = 0.35$ in Eq. (3) and this has been employed as the fourth alternative *Re-X* relationship in this study. A detailed summary of the *Re-X* relationship for the frozen hydrometeors is given by Rahman and Testik (2020).

Fourth, the mass of a snowflake was calculated from *Re-X* relationship for each size bin and is expressed as

$$m = \frac{\pi \eta^2 X}{8 g \rho_a} \left(\frac{A_e}{A}\right)^t \quad (4)$$

where g is the gravitational acceleration, A_e is the effective particle area, and A is the area of the smallest circle or ellipse which contains A_e. The area ratio (A_e/A), which is equal to $(D_{eq}/D_{mx})^2$, is 0.69, 0.59, 0.51, and 0.44 for α = 1.2, 1.3, 1.4, and 1.5, respectively. The exponent t in Eq. (4) is equal to 0.25 for the BM, MH, and KC methods, and is 0.5 for the HW method.

Mirroring the approach of Tokay et al. (2022), the mass of a snowflake (m) has also been expressed as a function of D_{mx} via a power law fit. The power law fit was applied to $m(D_{mx})$ relationships using orthogonal least squares and is expressed as;

$$m = a_m \, D_{mx}^{bm} \quad (5)$$

The coefficient and exponent in Eq. (5) are fitted using the bin-median snowflake mass, in grams, and the D_{mx} bin midpoint value in millimeters. The fitting is only applied if there are at least eight bins that contained 10 or more data points each.

b. Particle Size distribution (PSD)

The PSD is defined as the number of particles per unit volume of air in a given D_{eq} size interval. As the true sampling volume of the PIP depends on the particle size (recall that particles that touch the edge of the image are ignored) and sampling period, the DOF and FOV for a given particle size and the sampling period, T, over which the PSD is being computed will factor into the PSD calculation. As such, the PIP PSD for the i^{th} size interval is formulated as

$$N\left(D_{eq,i}\right) = \frac{1}{TN_f \Delta D_{eq,i}} \sum_{j=1}^{N} \frac{1}{DOF_{i,j} FOV_{i,j}} \quad (6)$$

where N_f is the number of frames and ΔD_{eq} is the width of the PSD size bin. For this study, the typical value of T is 60 seconds; PIP captures 380 frames per second, providing the value of N_f; ΔD_{eq} is 0.2 mm; the FOV in square meters is approximately FOV = $10^{-6}(48 - D_{eq})(64 - D_{eq})$, where D_{eq} is expressed in mm; and DOF in meters is approximately DOF = $(0.117/2) D_{eq}$, with D_{eq} again expressed in mm.

The three-parameter gamma distribution has widely been used in atmospheric sciences community and is expressed as

$$N(D_{eq}) = N_0 D_{eq}^{\mu} \exp(-\Lambda D_{eq}) \quad (7)$$

where N_0, Λ, and μ are the intercept, slope, and shape parameters, respectively, and D_{eq} is the volume equivalent diameter of falling snow, which is the same as the Waddel disk diameter described above. The concept of the normalized gamma size distribution was discussed and later adopted in the scientific community following the pioneering work by Testud et al. (2001) even though it was first introduced by Willis (1984). The normalization allows the use of physical quantities of size distribution such as total concentration, N_T, liquid water content, W, and D_{mass}.

This study uses the normalized gamma size distribution with respect to W and D_{mass} and is expressed as

$$N(D_{eq}) = N_W f(\mu) \left(\frac{D_{eq}}{D_{mass}}\right)^{\mu} \exp\left[-(\mu + b_m + 1)\frac{D_{eq}}{D_{mass}}\right] \quad (8)$$

where D_{mass} is expressed as,

$$D_{mass} = \frac{\int_{D_{min}}^{D_{max}} m(D_{mx}) D_{eq} N(D_{eq}) dD_{eq}}{\int_{D_{min}}^{D_{max}} m(D_{mx}) N(D_{eq}) dD_{eq}} \quad (9)$$

where D_{min} and D_{max} are the minimum and maximum particle size, respectively. Assuming $D_{min} = 0$ and $D_{max} = \infty$, and the mass-diameter relationship from Eq. (5), the Eq. (9) becomes

$$D_{mass} = \frac{(\mu+b_m+1)}{\Lambda} \quad (10)$$

The f(μ) is a dimensionless quantity and is expressed as,

$$f(\mu) = \frac{(\mu+b_m+1)^{\mu+b_m+1}}{\Gamma(\mu+b_m+1)} \quad (11)$$

N_W is the normalized intercept parameter in units of m^{-3} mm^{-1} and is expressed as

$$N_W = \frac{W}{a_m^* D_{mass}^{(b_m+1)}} \quad (12)$$

where $a_m^* = a_m \alpha^{bm}$ in units of g mm^{-bm}. W is in units of g m^{-3} and is given as,

$$W = \int_{D_{min}}^{D_{max}} m(D_{mx}) N(D_{eq}) dD_{eq} \quad (13)$$

If Eq. (12) adopts the standard gamma function Eq. (7) with $D_{min} = 0$ and $D_{max} = \infty$ first, and then uses the conversion between Λ and D_{mass} in Eq. (10), it becomes

$$W = N_0 a_m^* \frac{\Gamma(\mu+b_m+1)}{\Lambda^{(\mu+b_m+1)}} = N_0 a_m^* \frac{\Gamma(\mu+b_m+1)}{(\mu+b_m+1)^{(\mu+b_m+1)}} D_{mass}^{(\mu+b_m+1)} \quad (14)$$

Eqs. (10) and (14) show the transformations between the standard and normalized gamma distribution parameters, respectively.

c. Shape Parameter (μ)

393 The shape parameter of the gamma PSD has a wide range due to the inherent variability of
394 the size spectrum and the boundaries are determined based on the method used to calculate
395 the distribution. McFarquhar et al. (2015) presented five different methods to determine
396 the parameters of gamma distribution. The shape parameter ranged from 1.62 to 2.60 for a
397 given sample PSD in their study. Tokay et al. (2016, 2017), on the other hand, determined
398 the shape parameter by minimizing the root-mean-square difference between the observed
399 and gamma PSD-based rain rate. They showed that the probability distribution of μ ranges
400 from -2 to 20 with a mode between 2 and 4.
401
402 This study uses a different methodology. Rather than minimizing the difference between the
403 observed and gamma PSD based bulk descriptors of snowfall, the Mean Fractional Bias (MFB)
404 between the PIP- and gamma PSD-based bulk descriptors of snowfall is calculated for $-2 \leq \mu$
405 ≤ 10 range with an increment of one. The MFB is given as,
406
407 $$MFB = \frac{1}{N}\sum_{i=1}^{N}\frac{(P_{est,i}-P_{obs,i})}{P_{obs,i}} \quad (15)$$
408
409 where P is one of the bulk parameters of the snowfall such as N_T, SWE or Ze and where P_{obs}
410 is calculated from PIP observations and or P_{est} is computed from the gamma PSD parameters.
411 The sample size, N, exceeds 6,000-7,000 depending on the choice of bulk descriptors of
412 snowfall. The minimum sample size thresholds to derive the $m(D_{mx})$ relationship explained
413 above contributed to the differences in the sample size in calculating the MFB. The standard
414 deviation of the mean fractional bias was also included in the analysis.
415
416 This method not only provides the best μ for a given range but also provides the level of
417 accuracy for the prescribed μ values as in the GPM DPR and combined algorithms. The bulk
418 descriptors of interest are N_T, SWER, Ze at Ku-band, and DFR. These quantities are a function
419 of different moments of the PSD and therefore are sensitive to the different intervals of the
420 size distribution. The snowfall rate (SR), the intensity of falling snow, is also needed to
421 calculate the bulk density, which is given as
422

$$\rho_{snow} = \rho_w \frac{SWER}{SR} \quad (16)$$

where ρ_w is the density of water in g cm^{-3}.

The total concentration of the particles within a volume of air, N_T, in units of m^{-3}, is expressed as,

$$N_T = \int_{D_{min}}^{D_{max}} N(D_{eq}) dD_{eq} \quad (17)$$

The SR is a measure of the intensity of falling snow and is expressed as functions of equivalent particle volume, concentration, and fall velocity and is given in units of mm h^{-1} for a given minute as follows:

$$SR = 6\,\pi\,10^{-4} \int_{D_{min}}^{D_{max}} v(D_{mx}) D_{eq}^3 N(D_{eq}) dD_{eq} \quad (18)$$

The SWER is the liquid equivalent rate of falling snow and is expressed as functions of mass, fall speed, and concentration of the particles in a volume of air and is in units of mm h^{-1} for a given minute:

$$SWER = \frac{3.6}{\rho_w} \int_{D_{min}}^{D_{max}} m(D_{mx}) v(D_{mx}) N\left(D_{eq}\right) dD_{eq} \quad (19)$$

The Ze is the equivalent radar reflectivity factor and is expressed as a function of backscattering cross section (σ_{bscat}) and concentration of the particles in a volume of air. It is calculated for Ku-band and Ka-band wavelengths (λ = 2.17 cm, and 0.86 cm) using Mie Theory (Liao et al. 2013) and is formulated as

$$Ze(\lambda) = \frac{10^6 \lambda^4}{|K_w|^2 \pi^5} \int_{D_{min}}^{D_{max}} \sigma_{bscat}(D_{mx}, \lambda) N\left(D_{eq}\right) dD_{eq} \quad (20)$$

where $|K_W|^2$ is the dielectric constant of water and is 0.925 and 0.880 for Ku- and Ka-band, respectively.

The DFR is the dual-frequency ratio of Ze at Ku-band to Ze at Ka-band and is formulated as

$$DFR = 10\ log_{10}(\frac{Ze_{ku}}{Ze_{ka}}) \quad (21)$$

It should be noted that the Mie scattering based σ_{bscat} is underestimated at Ka-band, in the presence of large particles (D_{eq} > 5 mm) (Tyynela et al. 2015) at low bulk densities (ρ_{snow} < 0.05 g cm^{-3}) (Liao and Meneghini, 2022). This means DFR is overestimated under these conditions. In this study, the focus is the general impact on DFR with changes in the PSD parameters rather than a quantitative assessment. These qualitative changes remain the same irrespective of whether the sphere or spheroid model is adopted.

4. Results

The findings of this study are presented by a) histograms of D_{mass} versus log(N_W) and b) mean fractional bias of the shape parameter of gamma PSD. These two sets of results address two objectives of the study defined above.

a. D_{mass} vs. log(N_W) histogram

This section presents two-dimensional (2-D) histograms of D_{mass} and log(N_W) for four different *Re-X* relationships and for different D_{mx}-D_{eq} relationships based on PIP observations during ICE-POP 2018 (Figure 2). The combined PIP observations created a rich data set that is adequate for the purpose of this study. The event-to-event variability of the 2-D histograms of D_{mass} and log (N_W) for a given *Re-X* and D_{mx}-D_{eq} relationship (not shown) demonstrates the diversity of the snowfall characteristics though not necessarily the full diversity of global snowfall.

The 2-D histograms of D_{mass} and $\log(N_W)$ are generated as 40 x 40 matrices between 0 and 4 mm and between 1 and 5 $\log(mm^{-1}\ m^{-3})$ with a 0.1 unit increment for both parameters, respectively. The general trend with high particle concentrations [$\log(N_W) > 2.5\ \log(mm^{-1}\ m^{-3})$] at low D_{mass} (< 0.7 mm) and low particle concentrations [$\log(N_W) \leq 2.5\ \log(mm^{-1}\ m^{-3})$] at high D_{mass} (> 3.2 mm) was evident in all sixteen histograms (Figure 2). The peak concentrations were bounded between 0.9 and 1.5 mm for D_{mass} and between 3.0 and 3.5 $\log(mm^{-1}\ m^{-3})$ for $\log(N_W)$ in these histograms. Similar trends were previously reported for rain using 2DVD observations (Figure 4 of Tokay et al. 2020) and for snow using PARSIVEL[2] observations (Figure 5 of Yu et al. 2020) but the range of D_{mass} and $\log(N_W)$ values were different in those studies.

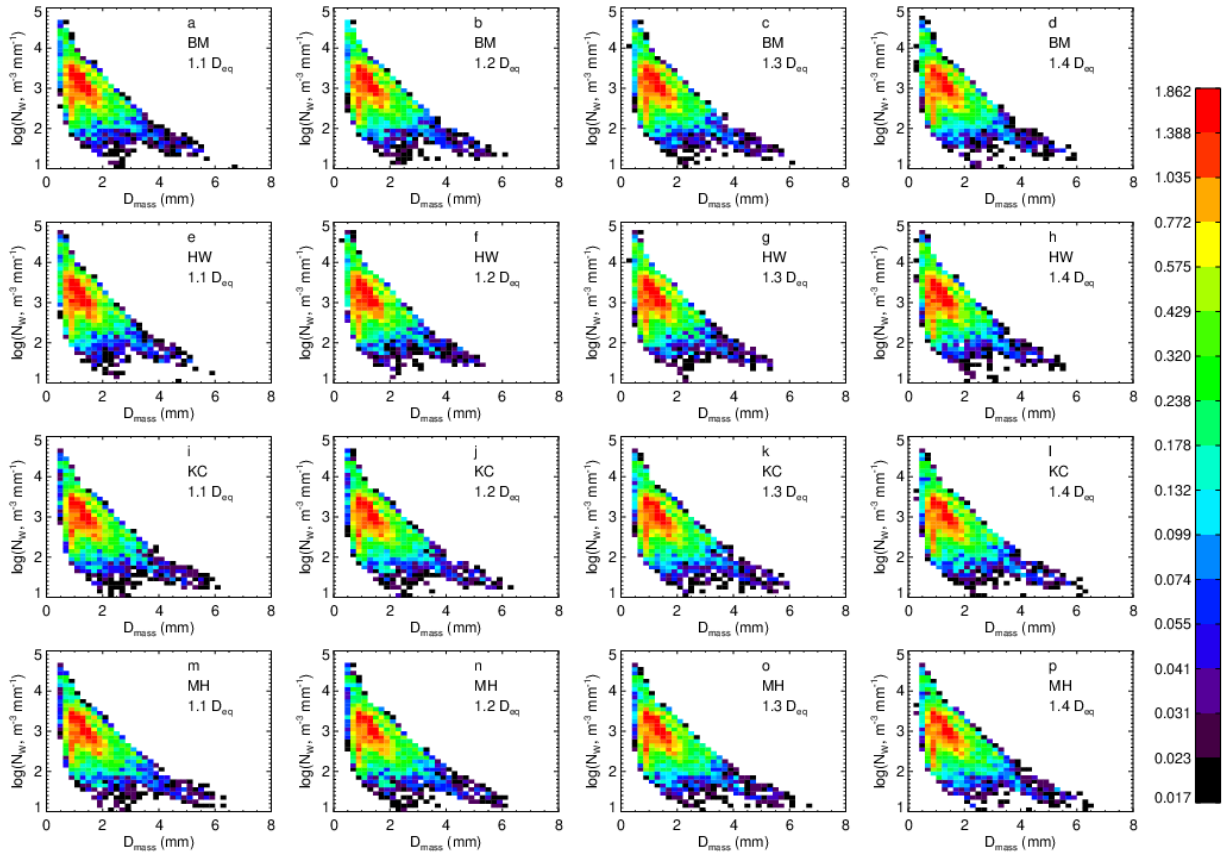


Figure 2. Two-dimensional histogram of D_{mass} versus $\log(N_W)$ for four different D_{mx}-D_{eq} relationships and four different *Re-X* relationships (BM, HW, KC, MH). The colorbar shown on the right side represents the percent occurrence for all sixteen diagrams and is in a logarithmic scale.

497

498 The differences between the sixteen histograms were minimal. The median and maximum
499 D_{mass} were lower for the HW method among the *Re-X* relationships and the maximum D_{mass}
500 was higher for $1.4D_{eq}$ among the D_{mx}-D_{eq} relationships (Table 1). In contrast, the median and
501 maximum $\log(N_W)$ were higher for the HW method among the *Re-X* relationships but there
502 were no noticeable differences in the maximum $\log(N_W)$ among the D_{mx}-D_{eq} relationships
503 (Table 2).

504

505 Table 1. D_{mass} statistics in mm units. The minimum, median, and maximum values for four different *Re-X*
506 relationships (BM, HW, KC, and MH) and for different D_{mx}-D_{eq} relationships. The sample size is 7799.
507

Re-X relations	$D_{mx}=1.1_{Deq}$	$D_{mx}=1.2D_{eq}$	$D_{mx}=1.3D_{eq}$	$D_{mx}=1.4D_{eq}$
BM	0.48, 1.23, 4.00	0.47, 1.23, 4.00	0.47, 1.24, 4.07	0.47, 1.25, 4.08
HW	0.46, 1.15, 3.69	0.46, 1.16, 3.70	0.46, 1.17, 3.74	0.46, 1.17, 3.80
KC	0.49, 1.28, 4.25	0.48, 1.29, 4.24	0.48, 1.30, 4.29	0.48, 1.29, 4.33
MH	0.49, 1.30, 4.39	0.49, 1.31, 4.38	0.48, 1.31, 4.42	0.48, 1.31, 4.47

508

509

510 Table 2. N_W statistics in $\log(m^{-3}\ mm^{-1})$ units. The minimum, median, and maximum values for four
511 different *Re-X* relationships (BM, HW, KC, and MH) and for different D_{mx}-D_{eq} relationships. The sample
512 size ranges between 6965-7471.
513

Re-X relations	$D_{mx}=1.1_{Deq}$	$D_{mx}=1.2D_{eq}$	$D_{mx}=1.3D_{eq}$	$D_{mx}=1.4D_{eq}$
BM	1.54, 2.95, 4.29	1.55, 2.94, 4.32	1.54, 2.94, 4.32	1.54, 2.93, 4.31
HW	1.67, 3.04, 4.35	1.66, 3.03, 4.39	1.65, 3.02, 4.38	1.65, 3.02, 4.38
KC	1.47, 2.88, 4.23	1.46, 2.87, 4.27	1.46, 2.87, 4.27	1.45, 2.87, 4.25
MH	1.42, 2.85, 4.22	1.42, 2.85, 4.25	1.41, 2.85, 4.26	1.41, 2.84, 4.25

514

515 The dependency of the 2-D histogram of D_{mass} and $\log(N_W)$ on ρ_{snow}, Ze_{Ku}, and DFR are shown
516 for BM based *Re-X* relationship and D_{mx} = 1.2 D_{eq} (Figure 3). For bulk density, there is
517 minimal dependency on $\log(N_W)$ but there is a clear trend of increasing ρ_{snow} with decreasing
518 D_{mass} (Figure 3a). For Ze_{Ku}, there is an increasing trend with both D_{mass} and $\log(N_W)$ (Figure

3b), which is consistent with the rain study of Tokay et al. (2020). As shown in Figure 3c, the DFR increases monotonically with D_{mass} and, consistent with the definition of this quantity, is essentially independent of $\log(N_W)$. The slight variations of DFR with respect to $\log(N_W)$ are due to the averaging procedure where each pixel value is calculated for 0.2 D_{mass} interval.

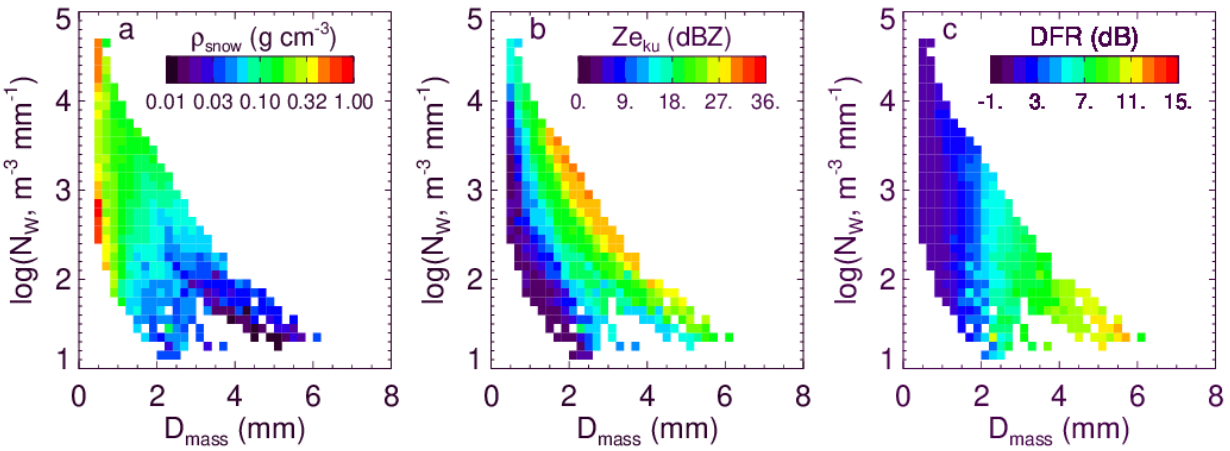


Figure 3. Two-dimensional distribution of D_{mass} versus $\log(N_W)$ as a function of a) mean bulk density, ρ_{snow}, b) Ku-band reflectivity, Ze_{ku}, c) dual frequency ratio, DFR for D_{mx} = 1.2 D_{eq} D_{mx}-D_{eq} and BM *Re-X* relationship. Note the use of a logarithmic scale for the color bar in panel a.

An empirical relationship between the parameters of the gamma PSD has been suggested for retrieving the PSD parameters from dual-polarization and dual-frequency radar measurements (Zhang et al. 2003). For D_{mass} and $\log(N_W)$, it is clear that there would be a large scatter for both parameters if an empirical relationship is derived between the two parameters. Liao et al. (2020) normalized the rain rate (R) by N_W and obtained the following power law relationship: $R/N_W = 1.588 \times 10^{-4}\ D_{mass}^{4.706}$. This relationship is virtually unchanged for the four different μ values (0, 3, 6, and 10). The additional information, R in this case, substantially reduced the scatter about D_{mass}.

This study normalizes both SWER and W by N_W. Both SWER and W are functions of particle mass, which is calculated based on fall velocity measurements. The SWER is also a function of fall velocity as shown in Eq. (19). Unlike in rain, there is no single relationship between the fall velocity and particle size for snow and there is a wider variability in fall velocity for

a given size depending on particle habit and composition. For the pair of BM *Re-X* relationship and $D_{mx} = 1.2\ D_{eq}$, the following expression was found between $SWER/N_W$ and D_{mass} using an orthogonal distance regression (Boggs et al. 1992),

$$SWER/N_W = 4.030 \times 10^{-4}\ D_{mass}^{2.598} \qquad (22)$$

The spread in $SWER/N_W$ is wide reaching 24 gate spacing in $SWER/N_W$ at D_{mass} = 1 mm. Despite the scatter, the power law fit was representative of the most of the observations (Figure 4a). The distribution of $SWER/N_W$ split at D_{mass} > 4 mm. These two modes associate with the cold and warm low events. The merged warm low and air-sea interaction database is associated with the higher segment, while the lower segment is associated with the merged cold low database (not shown). High bulk density observations coincided with the low D_{mass} and high $SWER/N_W$ region, while the high D_{mass} and low $SWER/N_W$ region coincide with the low bulk density observations (Figure 4b). High Ze_{Ku} and high DFR observations were found in high $SWER/N_W$ and in high D_{mass} regions, respectively (Figures 4c, 4d).

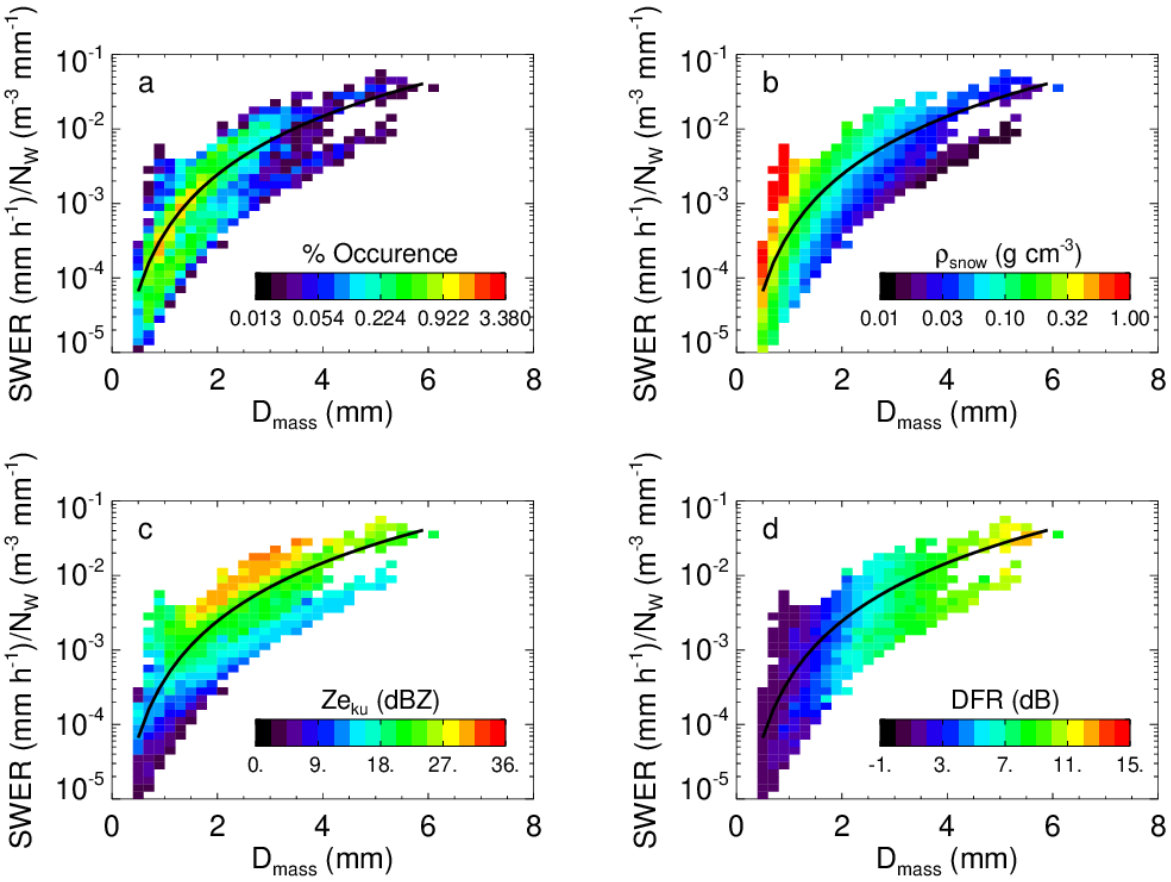


Figure 4. Two-dimensional distribution of D_{mass} versus SWE/N_W as a function of a) percent occurrence, b) mean bulk density, ρ_{snow}, c) Ku-band reflectivity, Ze_{Ku}, d) dual frequency ratio, DFR for $D_{mx} = 1.2\ D_{eq}$ and BM *Re-X* relationship. The best fit line between D_{mass} and $SWER/N_W$ following Eq. (22) is also shown. Note the use of a logarithmic scale for the color bar in panel a.

For the same pair of *Re-X* and D_{mx}-D_{eq} relationships, the following expression was found between W/N_W and D_{mass} using an orthogonal regression,

$$W/N_W = 1.154 \times 10^{-4}\ D_{mass}^{2.544} \qquad (23)$$

The spread along the W/N_W is relatively narrow reaching 15 gate spacing in W/N_W at D_{mass} = 1 mm and the power law fit represents the vast majority of the observations (Figure 5a). Similar to the SWER normalization, there are two modes of W/N_W distribution at D_{mass} > 4 mm (Figure 5a) and low ρ_{snow} observations coincide with the high D_{mass} and high W/N_W

region (Figure 5b). The high Ze_{ku} and DFR observations are found in the region of high W/N_W and high D_{mass}, respectively (Figures 5c, 5d).

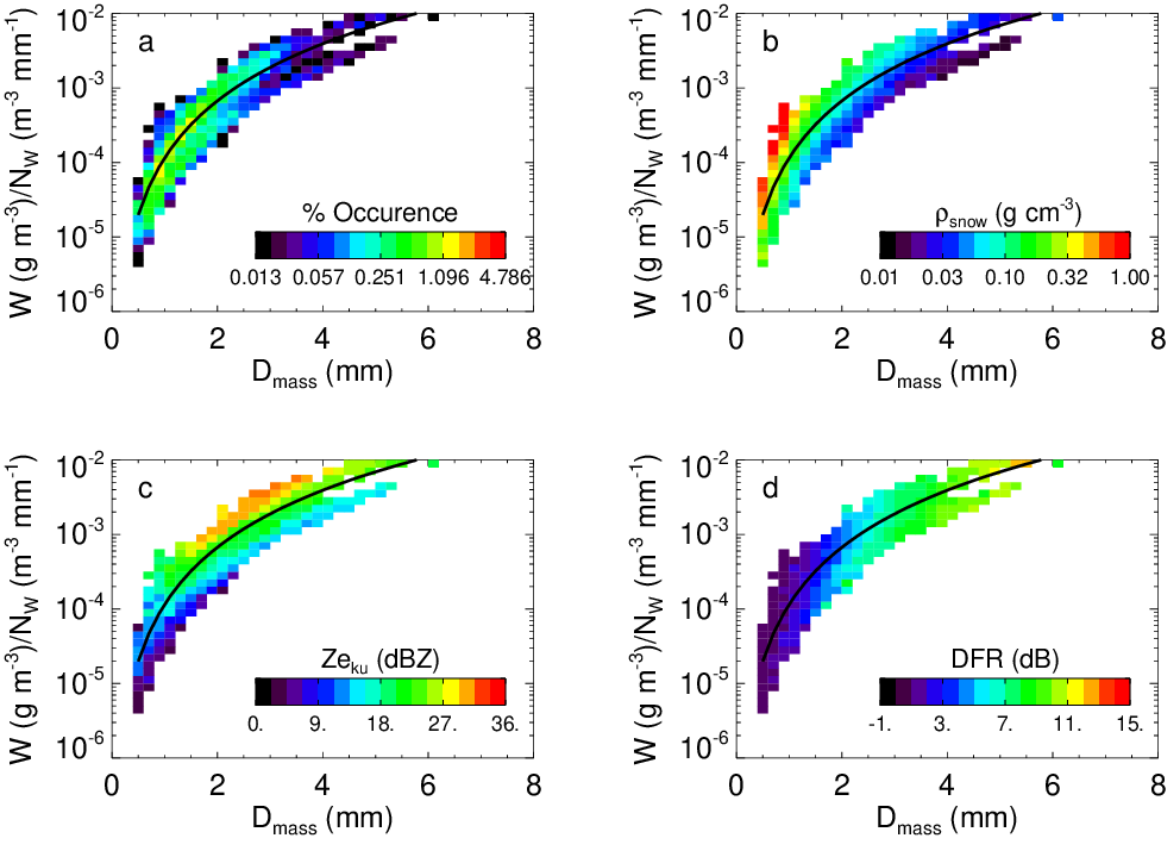


Figure 5. Two-dimensional distribution of D_{mass} versus W/N_W as a function of a) percent occurrence, b) mean bulk density, ρ_{snow}, c) Ku-band reflectivity, Ze_{Ku}, d) dual frequency ratio, DFR for $D_{mx} = 1.2\ D_{eq}$ and BM *Re-X* relationship. The best fit line between D_{mass} and W/N_W following Eq. (23) is also shown.

The coefficients and exponents of Eqs. (22) and (23) were slightly different for the other pairs of *Re-X* and D_{mx}-D_{eq} relationships but relatively more sensitive to *Re-X* relationships used in this study. In particular, the two-dimensional histograms of $SWER/N_W$ and D_{mass} as well as W/N_W and D_{mass} in HW *Re-X* relationship had relatively more compact range for both variables. The spreads along the $SWER/N_W$ and W/N_W were 22 and 14 gate spacing, respectively. The coefficients and exponents in Eqs. (22) and (23) are lower when HW *Re-X* relationships are considered.

590 b. Performance of shape parameter (μ)

591

592 This section presents the characteristics of μ of normalized gamma PSD with respect to N_W
593 and D_{mass}. The objective is to address two questions: 1) What is the μ within the expected
594 range $-2 \le \mu \le 10$ that best satisfies the four different bulk parameters of snowfall (N_T, SWER,
595 Ze_{Ku}, and DFR); and 2) What is the error if μ, for snow, is prescribed as it has been in the
596 GPM combined radiometer radar ($\mu = 2$) and DPR ($\mu = 3$) algorithms? For the GPM
597 algorithms, Ze_{Ku} and DFR are retrieved from measured reflectivity after the attenuation
598 correction, while N_T and SWER are the retrieved from PSD parameters. The retrieval of PSD
599 parameters, D_{mass} and N_W, was shown in a flow chart of DPR algorithm in Figure 2 of Seto et
600 al. (2021). The MFB described in Eq. (15) is used for answering these two questions. To be
601 consistent with the previous section, Figure 6 is plotted for the combination of $D_{mx} = 1.2\ D_{eq}$
602 and BM *Re-X* relationship. The standard deviation of the MFB is also included in the analysis.
603 The trend of MFB with μ is the same for the other *Re-X* and D_{mx}-D_{eq} relationships, which are
604 included in the discussion.

605

606

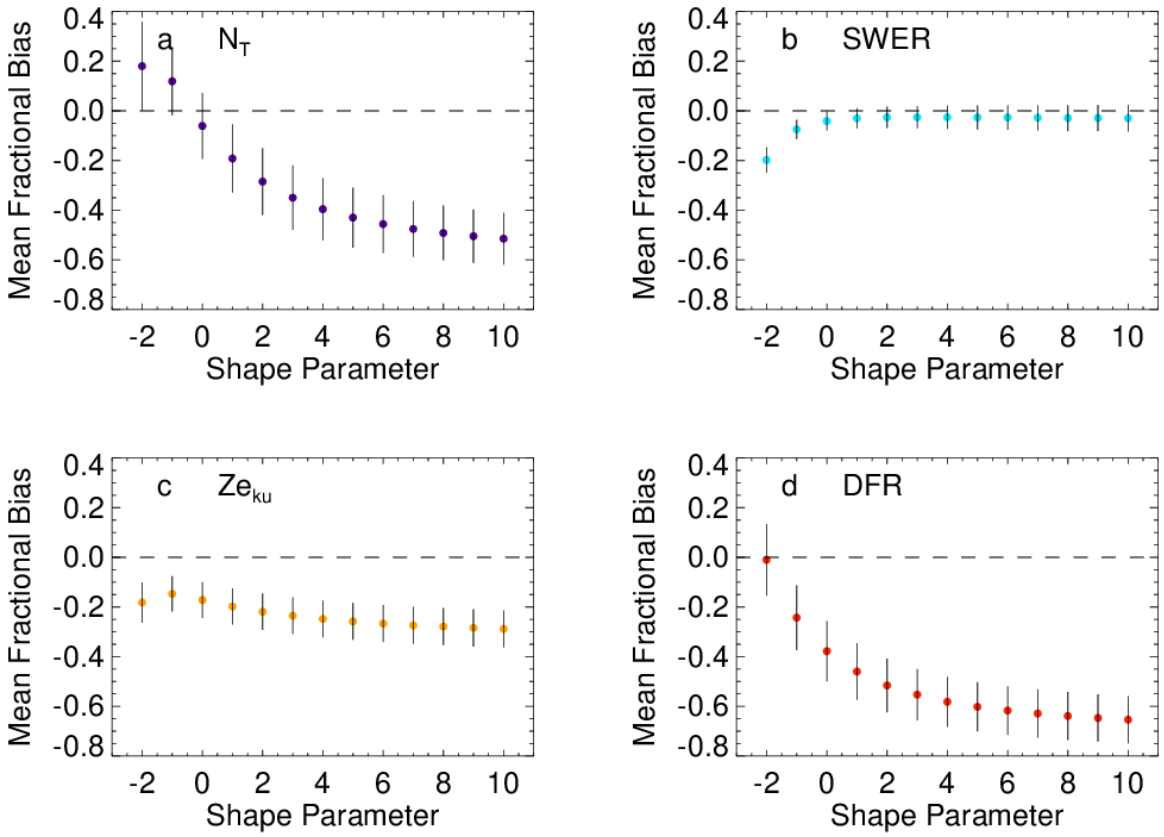


Figure 6. Mean Fractional Bias (MFB) of a) total concentration, N_T, b) snow water equivalent rate, SWER, c) Ku-band reflectivity, Ze_{Ku}, and d) dual frequency ratio, DFR. The bias is the difference when these integral parameters were calculated from PIP observed PSD and from gamma PSD parameters with prescribed shape parameter, μ. The standard deviation of the MFB is shown in vertical bars where filled circle represents the mean.

The μ = 0 had the best performance for all sixteen pairs of *Re-X* and D_{mx}-D_{eq} relationships when N_T is the bulk parameter. The N_T was underestimated when μ ≥ 0 while it was overestimated when μ < 0. When μ = 0, the MFB of N_T was -0.05 and ranged from 0.18 at μ = -2 to 0.51 at μ = 10 in Figure 6a. For all sixteen pairs of *Re-X* and D_{mx}-D_{eq} relationships, the range of MFB of N_T was 0.23-0.33 when μ = 2 and by 0.30-0.40 when μ = 3. The combination of HW *Re-X* and 1.4D_{eq} D_{mx}-D_{eq} relationship had the lowest MFB, while the highest MFB was observed for the combination of MH *Re-X* and 1.1D_{eq} D_{mx}-D_{eq} relationship. Since the GPM algorithms derive the PSD parameters from Ze measurements, it is expected to have a large error in N_T which is proportional to the zero moment of the size distribution. This study is able to quantify the error and provide a reference to the algorithm developers.

The $\mu = 3$ had the best performance for all sixteen pairs of *Re-X* and D_{mx}-D_{eq} relationships when SWER is the bulk parameter. The SWER was underestimated over the entire range of μ and the absolute value of the MFB was less than 0.04 when $\mu \geq 1$ for all sixteen pairs of *Re-X* and D_{mx}-D_{eq} relationships. The MFB of SWER was -0.03 at $\mu = 3$ and was substantially lower for $\mu < 0$ in Figure 6b. For $\mu = 2$ and $\mu = 3$, the MFB of SWER was between -0.02 and -0.03 for all sixteen pairs of *Re-X* and D_{mx}-D_{eq} relationships. This suggests that the dependence of SWER on μ is small in general and can be neglected as a source of significant error in the GPM algorithms.

The $\mu = -1$ had the best performance for all sixteen pairs of *Re-X* and D_{mx}-D_{eq} relationships when Ze_{ku} is the bulk parameter. Among the four bulk parameters, Ze_{Ku} had the least sensitivity to μ where the difference in MFB was ≤ 0.02 for $-2 \leq \mu \leq 10$. Ze_{Ku} was underestimated for the entire μ range. The MFB of Ze_{Ku} was -0.14 at $\mu = -1$ in Figure 6c and this was the highest among the four bulk parameters presented here. The MFB of Ze_{Ku} was -0.19 at $\mu = -2$ and its absolute value first decreased and then increased for $\mu \geq 0$, reaching to 0.27 at $\mu = 10$ in Figure 6c. For $\mu = 2$ and 3, the MFB of Ze_{Ku} ranged from -0.19 to -0.21 and from -0.21 to 0.2, respectively.

The $\mu = -2$ had the best performance for all sixteen pairs of *Re-X* and D_{mx}-D_{eq} relationships when DFR is the bulk parameter and the MFB at this μ value ranged from <-0.01 to -0.06. Unlike the other bulk parameters, the minimum and maximum MFB of DFR occurred for HW *Re-X* and $1.3D_{eq}$ D_{mx}-D_{eq} relationship and MH *Re-X* and $1.4D_{eq}$ D_{mx}-D_{eq} relationship, respectively. The DFR was slightly underestimated with MFB of -0.01 at $\mu = -2$ but the underestimation increased substantially with the shape parameter reaching to MFB of -0.65 at $\mu = 10$ in Figure 6d. For $\mu = 2$ and $\mu = 3$, the DFR was substantially underestimated with the range of MFB between -0.48 and -0.53, and between -0.52 and -0.57, respectively. This finding shows that the DFR is the least accurately retrieved at $\mu = 2$ and $\mu = 3$.

5. Summary and Conclusions

The PIP observations from ICE-POP 2018 field campaign were used to derive the parameters of the normalized gamma PSD in snow. The objectives of this study are to provide a reference for the range of D_{mass} and $\log(N_W)$ observations in snow and to evaluate the performance of the prescribed μ of the gamma PSD.

This study showed that the D_{mass} ranged between 0.46-4.47 mm with median values of 1.15-1.31 mm depending on the pair of *Re-X* and D_{mx}-D_{eq} relationships. It is important to note that, D_{mass} represents the actual snow particles diameter rather than the melted equivalent diameter. The range of $\log(N_W)$ was from 1.41 to 4.39 $\log(m^{-3}\ mm^{-1})$ with median values of 2.84-3.03. The ρ_{snow} increased with decreasing D_{mass} and was nearly insensitive to the $\log(N_W)$. Higher values of Ze_{Ku} were found in the high D_{mass} and high $\log(N_W)$ region and lower Ze_{Ku} values were found in the low D_{mass} and low $\log(N_W)$ region. The DFR increased with D_{mass} and was insensitive to $\log(N_W)$ as expected based on its definition.

The wide range of values in both D_{mass} and $\log(N_W)$ demonstrate that there is no single relationship that can relate these two parameters accurately. However, using N_W as a normalization of SWER and W results in power law relationships of the form of $SWE/N_W = a1\ D_{mass}^{b1}$ and $W/N_W = a2\ D_{mass}^{b2}$, where a1, a2 coefficients and b1, b2 exponents were determined through orthogonal distance regression. The power law relationships represent the majority of the observations where the spread in $SWER/N_W$ was higher than that in W/N_W. This is caused by the fall velocity dependence of SWER where the fall velocity of snowflakes is highly variable even for a fixed size.

The optimum value of the shape parameter depends on the bulk parameter of interest. The retrieved parameters, N_T and SWER yielded the best performance at $\mu = 0$ and $\mu = 2$, respectively, while the measured parameters, Ze_{Ku} and DFR, had the best performance at $\mu = -1$ and $\mu = -2$, respectively. All four bulk parameters were underestimated for the optimum μ except for DFR, which was 0.1%. The SWER had ≤4% underestimation for $\mu \geq 0$ but the MFB was as low as -0.22 at $\mu = -2$. The Ze_{Ku} had 14% underestimation at its best μ, highest

among the four bulk parameters and had the least sensitivity to the changes in μ. The N_T and DFR showed the highest sensitivity across the μ spectrum. The range of MFB was 49% and 65% for those parameters, respectively. The sensitivity to the choice of D_{mx}-D_{eq} and *Re-X* relationships was minimal for all four bulk descriptors of snowfall.

It is important to determine the error margins when μ is prescribed as 2 and 3 in GPM's combined radiometer-radar and DPR algorithms, respectively. For these two μ values, the N_T was underestimated by as high as 33% and 40%, respectively. In contrast, SWER was underestimated by just 3%, the least among the four bulk parameters. The Ze_{Ku} was underestimated by as high as 22% at μ = 2 and 23% at μ = 3, while the underestimation was 54% at μ = 2 and 57% at μ = 3 as being the highest in DFR.

It should be noted that the bulk parameters presented here are directly derived from the PIP-based PSD observations. The errors in μ is therefore combination of uncertainty in PIP-based PSD measurements itself and deviations from gamma model size distribution. For the DPR algorithm, the PSD parameters, D_{mass}, and N_W, are derived from reflectivity measurements that are functions of the higher moment of the PSD. For falling snow, there is a fairly robust relationship between the DFR and D_{mass} (not shown) but the scatter around the best fit line is also considerable and results in errors in the estimated D_{mass}.

The variability of PSD parameters in vertical is considered as a topic for future study. The PSD parameters can be derived from vertically pointing radars and compared to the PIP-based measurements. This exercise will provide the guidance on the microphysical process (e.g. aggregation, accretion, sublimation) of falling snow between the cloud base and the ground.

Acknowledgments

First and foremost, acknowledgments go to Kwang Deun Ahn of Korean Meteorological Administration and GyuWon Lee of Kyungpook National University for the leadership during

ICE-POP 2018. Thanks to Kwonil Kim of Kyungpook National University for field work and data collection during ICE-POP 2018. Specifically, the authors thanks to South Korean colleagues for operating NASA's Precipitation Imaging Package and providing Vaisala WXT520 weather station database. Dr. Helms' contribution to this study was supported by an appointment to the NASA Postdoctoral Program at NASA Goddard Space Flight Center, administered by Universities Space Research Association under contract with NASA.

Data Availability

The data used in this study was extracted though a secure file transformation site where the IP address, the username and password were set by the ICE-POP 2018 field campaign organizers. To access the database please contact to Kwonil Kim (kwonil.kim.0@gmail.com).

Appendix

This appendix describes the variables that are used in this study. The variables include environmental, snowflake mass, particle size distribution, and integral snowfall parameters. The appendix also includes the variables that were mentioned but not used in this study.

T_{wb}: wet-bulb temperature.

D_{eq}: Equivalent diameter. It is a Waddel disk diameter that was described as the diameter of the disk with the same area as the particle in National Instruments IMage AQuisition (IMAQ) manual, which describes D_{eq} equal to $2(\text{area}/\pi)^{0.5}$, where area is the total area of shadowed pixels bounded by a box.

D_{min}: minimum particle size based on D_{eq} measurements.

D_{max}: maximum particle size based on D_{eq} measurements.

D_{mx}: maximum dimension of the particle. It is prescribed as a function of D_{eq} as in Eq. (1) in this study.

D_{mass}: mass weighted mean diameter.

744 D_{mass}*: melted mass weighted particle diameter.

745 N_0: intercept parameter of gamma particle size distribution.

746 Λ: slope parameter of the gamma particle size distribution.

747 μ: shape parameter of the gamma particle size distribution.

748 N_T: total particle concentration that is given as number of particle per cubic volume of air.

749 W: liquid water content.

750 N_W: normalized intercept parameter of gamma size distribution with respect to W and

751 D_{mass}.

752 v: median fall velocity of a snowflake.

753 m: mass of a snowflake.

754 a_m: coefficient of the $m(D_{mx})$ power-law relationship.

755 b_m: exponent of the $m(D_{mx})$ power-law relationship.

756 Re: Reynolds number.

757 η: dynamic viscosity

758 ρ_a: density of air at the ground level.

759 X: Best number.

760 δ_0: boundary layer thickness.

761 C_0: drag coefficient.

762 g: gravitational constant.

763 A_e: effective particle area.

764 A: the area of the smallest circle or ellipse which contains A_e.

765 ρ_W: density of water.

766 ρ_{snow}: bulk density of falling snow.

767 SR: snow rate. This is intensity of falling snow without melting.

768 SWER: melted equivalent snow rate.

769 SWE: melted equivalent of falling snow.

770 R: rain rate

771 PR: precipitation rate.

772 λ: radar wavelength.

773 σ_{bscat}: backscattering cross section

774 $|K_W|^2$: dielectric constant of water

775 Ze_{Ku}: radar reflectivity at Ku-band wavelength.

776 Ze_{Ka}: radar reflectivity at Ka-band wavelength.

777 DFR: dual frequency ratio.

778

779 References

780

781 Boggs, P. T., R. H. Byrd, J. E. Rogers, and R. B. Schnabel, 1992: User's reference guide for
782 ODRPACK version 2.01: Software for weighted orthogonal distance regression.
783 https://docs.scipy.org/doc/external/odrpack_guide.pdf.

784

785 Böhm, H., 1989: A general equation for the terminal fall speed of solid hydrometeors. J. Atmos.
786 Sci., 46, 2419–2427.

787

788 Chase, R. J., S. W. Nesbitt, and G. M. McFarquhar, 2020: Evaluation of the microphysical
789 assumptions within GPM-DPR using ground-based observations of rain and snow.
790 Atmosphere, 11, 619.

791

792 Gehring, J., A. Ferrone, A. C. Billault-Roux, N. Besic, K. D. Ahn, G. W. Lee, A. Berne, 2021: Radar
793 and ground-level measurements of precipitation by the Ecole Poytechnique Federale de
794 Laussane during the International Collaborative Experiments for PyongChang 2018 Olympic
795 and Paralympic winter games. Earth Syst. Sci. Data, 13, 417-433.

796

797 Grecu, M., W. S. Olson, S. J. Munchak, S. Ringerud, L. Liao, Z. Haddad, B. Kelley, and S.
798 McLaughlin, 2016: The GPM combined algorithm. J. Atmos. Oceanic Technol., 33, 2225– 2245,
799 https://doi.org/10.1175/JTECH-D-16-0019.1.

800

801 Helms, C. N., S. J. Munchak, A. Tokay, and C. Pettersen, 2022: A comparative evaluation of
802 snowflake particle size an shape estimation techniques used by the Precipitation Imaging
803 Package (PIP), Multi-Angle Snowflake Camera (MASC), and Two-Dimensional Video
804 Disdrometer (2DVD). Atmos Measu. Tech. (in review).

Heymsfield, A. J., and C. D. Westbrook, 2010: Advancements in the estimation of ice particle fall speeds using laboratory and field measurements, J. Atmos. Sci., 67, 2469–2482.

Iguchi, T., S. Seto, R. Meneghini, N. Yoshida, J. Awaka, M. Le, V. Chandrasekar, and T. Kubota, 2017: GPM/DPR level-2. JAXA Algorithm Theoretical Basis Doc., 68 pp., https://www.eorc.jaxa.jp/GPM/doc/algorithm/ATBD_DPR_201708_whole_1.pdf.

IMAQ, 2004: IMAQ Vision Concepts Manual. National Instruments. August 2004 Edition. Available online at www.ni.com.

Khvorostyanov, V., and J. A. Curry, 2005: Fall velocities of hydrometeors in the atmosphere: Refinements to a continuous analytical power law. J. Atmos. Sci., 62, 4343–4357.

Kim, K., W. Bang, E. C. Chang, F. J. Tapiador, C. L. Tsai, E. Jung, and G. W. Lee, 2021: Impact of wind pattern and complex topography on snow microphysics during ICE-POP 2018. Atmos. Chemistry Physics, https://doi.org/10.5194/acp-2021-128.

Kozu, T., T. Iguchi, T. Shimomai, and N. Kashiwagi, 2009: Raindrop size distribution modeling from a statistical rain parameter relation and its application to the TRMM precipitation radar rain retrieval algorithm. J. Appl. Meteor. Climatol., 48, 716-724.

Kulie, M. S., and co-authors, 2021: Snowfall in the Northern Great Lakes: Lessons leard from a multi-sensor observatory. Bull. Amer. Meteor. Soc., (accepted for publication).

Liao, L., R. Meneghini, H. K. Nowell, and G. Liu, 2013: Scattering computations of snow aggregates 1183 from simple geometrical particle models. IEEE J. Sel. Topics Appl. Earth Observ. Remote Sens., 6, 1184 1409-1417.

Liao, L., R. Meneghini, A. Tokay, and L. F. Bliven, 2016: Retrieval of snow properties for Ku- and Ka-band dual frequency radar. J. Atmos. Meteor. Climatol., 55, 1845-1858.

Liao, L., R. Meneghini, T. Iguchi, and A. Tokay, 2020: Characteristics of DSD bulk parameters: Implication for radar rain retrieval. Atmosphere, 11, 670; doi:10.3390/atmos11060670.

Liao, L., and R. Meneghini, 2022: GPM DPR retrievals: Algorithm, evaluation, and validation. Remote Sensing, 14(4), 843; https://doi.org/10.3390/rs14040843

McFarquhar G. M., T-L. Hsieh, M. Freer, J. Mascio, and B. F. Jewett, 2015: The characterization of ice hydrometeor gamma size distributions as volumes in N_0-λ-μ phase space: Implications for microphysical process modeling. J. Atmos. Sci., 72, 892-909.

Mitchell, D. L., and A. J. Heymsfield, 2005: Refinements in the treatment of ice particle terminal velocities, highlighting aggregates. J. Atmos. Sci., 62, 1637–1644.

Newman, A. J., P. A. Kucera, and L. F. Bliven, 2009: Presenting the Snowflake Video Imager (SVI), J. Atmos. Ocean. Tech., 26, 167–179.

Pettersen, C., M. S. Kulie, L. F. Bliven, A. J. Merrelli, W. A. Petersen, T. J. Wagner, D. B. Wolff, and N. B. Wood, 2020a: A composite analysis of snowfall modes from four winter seasons in Marquette, Michigan. J. Appl. Meteor. Climatol., 59, 103-124.

Pettersen, C., L. F. Bliven, N. B. Wood, A. Von Lerber, M. S. Kulie, M. E. Mateling, D. N. Moisseev, S. J. Munchak, W. A. Petersen, and D. B. Wolff, 2020b: Introducing the Precipitation Imaging Package: Assessment of microphysical and bulk characteristics of snow, Atmosphere, 11, 785.

Pettersen, C., L. F. Bliven, M. S. Kulie, N. B. Wood, J. A. Shates, J. Anderson, M. E. Mateling, W. A. Petersen, A. von Lerber, and D. B. Wolff, 2021: The precipitation imaging package: Phase partitioning capabilities. Remote Sensing, 13(11), 2183; https://doi.org/10.3390/rs13112183.

866 Petty, W. G., and W. Huang, 2011: The modified gamma size distribution applied to
867 inhomogeneous and non-spherical particles: Key relationships and conversions. J. Atmos.
868 Sci., 68, 1460-1473.
869
870 Rahman, K., and F. Testik, 2020: Shapes and fall speeds of freezing and frozen raindrops. J.
871 Hydrometeor., 21, 1311-1331.
872
873 Seto, S., T. Iguchi, and T. Oki, 2013: The basic performance of a precipitation retrieval
874 algorithm for the Global Precipitation Measurement mission's single/dual-frequency radar
875 measurements. IEEE Trans. Geosci. Remote Sens., 51, 5239–5251.
876
877 Seto, S., T. Iguchi, R. Meneghini, J. Awaka, T. Kubota, T. Masaki, and N. Takahashi, 2021: The
878 precipitation rate retrieval algorithms for the GPM dual-frequency precipitation radar. J.
879 Meteor. Soc. Japan, 99, 205-237.
880
881 Skofronick-Jackson, G., W. A. Petersen, W. Berg, C. Kidd, E. F. Stocker, D. B. Kirschbaum, R.
882 Kakar, S. A. Braun, G. J. Huffman, T. Iguchi, P. E. Kirstetter, C. Kummerow, R. Meneghini, R. Oki,
883 W. S. Olson, Y. N. Takayabu, K. Furukawa, and T. Wilheit, 2017: The Global Precipitation
884 Measurement (GPM) Mission for Science and Society. Bull. Amer. Meteor. Soc., 98, 1679–
885 1695.
886
887 Szyrmer, W., and I. Zawadzki, 2010: Snow studies. Part II: Average relationship between
888 mass of snowflakes and their terminal fall velocity. J. Atmos. Sci., 67, 3319–3335.
889
890 Tapiador, F. J., A. Villalba-Pradas, A. Navarro, E. García-Ortega, K.-S. S. Lim, K. Kim, K.D. Ahn,
891 G. Lee, 2021: Future Directions in Precipitation Science. Remote Sens.,13,
892 1074.https://doi.org/10.3390/rs13061074.
893
894 Testud, J., S. Oury, R. A. Black, P. Amayenc, and X. Dou, 2001: The concept of "normalized"
895 distribution to describe raindrop spectra: A tool for cloud physics and cloud remote sensing.
896 J. Appl. Meteor., 40, 1118-1140.

Tiira, J., D. N. Moisseev, A. von Lerber, D. Ori, A. Tokay, L. F. Bliven, and W. Petersen, 2016: Ensemble mean density and its connection to other microphysical properties of falling snow as observed in Southern Finland. Atmos. Meas. Tech., 9, 4825-4841.

Tokay, A., and P. G. Bashor, 2010: An experiment study of small-scale variability of raindrop size distribution. J. Appl. Meteor. Climatol., 49, 2348-2365.

Tokay, A., W. A. Petersen, P. Gatlin, and M. Wingo, 2013: Comparison of raindrop size distribution measurements by collocated disdrometers. J. Atmos. Oceanic Technol., 30, 1672–1690.

Tokay, A., L. P. D'Adderio, D. B. Wolff, and W. A. Petersen, 2016: A field study of pixel-scale variability of raindrop size distribution. J. Hydrometeor., 17, 1855–1868.

Tokay, A., L. P. D'Adderio, D. B. Wolff, and W. A. Petersen, 2017: A field study of footprint-space variability of raindrop size distribution. J. Hydrometeor., 18, 3165–3179.

Tokay, A., L. P. D'Adderio, D. B. Wolff, and W. A. Petersen, 2020: Development and evaluation of the raindrop size distribution parameters for the NASA Global Precipitation Measurement Mission Ground Validation Program. J. Atmos. Oceanic. Technol., 37, 115-128.

Tokay, A., A. von Lerber, C. Pettersen, M. S. Kulie, D. N. Moisseev, and D. B. Wolff, 2022: Retrieval of snow water equivalent by the Precipitation Imaging Package (PIP) over Northern Great Lakes. J. Atmos. Oceanic Technol., 39, 37-54.

Tyynela, J., J. Leinonen, D. Moisseev, and T. Nousiainen, 2015: Radar backscattering from snowflakes: Comparison of fractal, aggregate, and soft spheroid models. J. Atmos. Oceanic Technol., 28, 1365-1372.

927 von Lerber, A., D. Moisseev, F. Bliven, W. Petersen, A.-M. Harri, and V. Chandrasekar,
928 2017:Microphysical properties of snow and their link to Ze–S relations during BAECC 2014.
929 J. Appl. Meteor. Climatol., 56, 1561–1582.
930
931 Willis, P. T., 1984: Functional fits to some observed drop size distributions and
932 parameterization of rain. J. Atmos. Sci.,41, 1648–1661.
933
934 Yu, T., V. Chandrasekar, H. Xiao, and S. S. Joshil, 2020: Characteristics of particle size
935 distribution in the PyeongChang region of South Korea. Atmosphere, 11, 1093;
936 doi:10.3390/atmos11101093.
937
938
939